Discover Nano

Research

Optimization of process parameters in 3D-nanomaterials printing for enhanced uniformity, quality, and dimensional precision using physics-guided artificial neural network

Anita Ghandehari[1,2,3] · **Jorge A. Tavares-Negrete**[2,3,4] · **Jerome Rajendran**[1,2,3] · **Qian Yi**[1,3] · **Rahim Esfandyarpour**[1,2,3,4,5]

Received: 30 August 2024 / Accepted: 27 November 2024
Published online: 16 December 2024

Abstract
Pneumatic 3D-nanomaterial printing, a prominent additive manufacturing technique, excels in processing advanced materials like MXene, crucial for applications in nano-energy, flexible electronics, and sensors. A key challenge in this domain is optimizing process parameters—applied pressure, ink concentration, nozzle diameter, and printing velocity—to achieve uniform, high-quality prints with the desired filament diameter. Traditional trial-and-error methods often result in significant material waste and time consumption. To address this, our study introduces a comprehensive pipeline that initially assesses whether the selected process parameters yield uniform, high-quality MXene prints. Subsequently, it employs a Physics-Guided Artificial Neural Network (PGANN) to predict the filament diameter based on these parameters, integrating fundamental physical principles of the printing process with experimental data. Our findings demonstrate that using an XGBoost classifier, we can classify printed filament quality with an accuracy of 90.44%. Furthermore, the PGANN model shows exceptional performance in predicting the filament diameter, achieving a Pearson Correlation Coefficient (PCC) of 0.9488, a Mean Squared Error (MSE) of 0.000092 mm^2, and a Mean Absolute Error (MAE) of 0.00711 mm. This pipeline significantly streamlines the process for researchers, facilitating the selection of optimal printing parameters to consistently achieve high-quality prints and accurately produce the desired filament diameter tailored to specific applications.

Keywords Additive manufacturing · 3D-nanomaterial printing · MXene · Process parameters · Physics-guided artificial neural network · Machine learning · Data-driven

1 Introduction

Pneumatic extrusion 3D-nanomaterial printing, a form of direct ink writing (DIW) in additive manufacturing, has emerged as a multipurpose technology with several advantages, including cost-effectiveness, rapid prototyping, and potential for high throughput [1–6]. This technology finds applications across various fields, such as biomedical

Supplementary Information The online version contains supplementary material available at https://doi.org/10.1186/s11671-024-04155-w.

✉ Rahim Esfandyarpour, rahimes@uci.edu | [1]Department of Electrical Engineering and Computer Science, University of California, Irvine, CA 92697, USA. [2]Henry Samueli School of Engineering, University of California, Irvine, CA 92697, USA. [3]Laboratory for Integrated Nano Bio Electronics Innovation, The Henry Samueli School of Engineering, University of California, Irvine, CA 92697, USA. [4]Department of Biomedical Engineering, University of California, Irvine, CA 92697, USA. [5]Department of Mechanical and Aerospace Engineering, University of California, Irvine, CA 92697, USA.

engineering, nanoengineering, and nanotechnology [7–12]. It inherits the general benefits of additive manufacturing, notably enhanced control over the volume and placement of extruded materials, establishing itself as the preferred technology for processing advanced nanomaterials [13, 14].

Among these advanced materials, MXene a two-dimensional (2D) transition nanomaterial with outstanding triboelectric, conductivity, and flexible properties has been processed with extrusion-based 3D nanomaterial printers [15]. Nonetheless, MXene's highly reactive surface akin to transition metal oxides combined with the functional groups (-F, =O, -OH) that provide linking sites, renders MXene promising material with applications in nano-energy production, flexible electronics, and wearable sensors. The 3D-nanomaterial printing of MXene requires uniform high-quality printing and precise control of the filament diameter to print uniform, conductive, precise, flexible, and microscale sensors and circuits [15].

Uniform prints are defined as achieving consistent quality without defects. To control the diameter of the nanomaterial printed filament and maintain its uniformity, fine-tuning process parameters of pneumatic printing is essential. The most influential process parameters during pneumatic printing include adjusting applied pressure, material viscosity, nozzle diameter, and the velocity at which the extruder moves [13, 16–19]. Currently, researchers are facing a significant challenge in identifying the optimal process parameters for a specific filament diameter with uniform quality. They often resort to a trial-and-error approach to ensure the filament produced is uniform and matches the desired diameter [20]. Such a method, however, leads to considerable consumption of time and materials as researchers iteratively adjust and test process parameters to achieve defect-free printing with the desired filament diameter. This iterative optimization process underscores the need for a more efficient strategy in the calibration of 3D-nanomaterial printing process parameters to enhance printing quality.

In this context, machine learning (ML) emerges as a powerful tool for enhancing the calibration of 3D printing process parameters. Fu et al., developed a Support Vector Machine (SVM) model, producing a process map aimed at aiding the selection of the best printing parameters to consistently achieve high-quality prints with a probability greater than 75% [21]. Tamir et al., combined open-loop and closed-loop ML models with a fuzzy system to optimize 3D printing parameters, improving print quality in additive manufacturing [22]. Deswal et al. optimized a process for enhancing the dimensional preciseness of fused deposition modeling (FDM) 3D printing. They applied hybrid statistical techniques, including response surface methodology combined with a genetic algorithm (RSM-GA), artificial neural networks (ANN), and a fusion of artificial neural networks and genetic algorithm (ANN-GA) [23]. Jeong et al., investigated the Aerosol Jet Printing (AJP) process, focusing on how its process parameters affect line width and resistivity. They established an operability window that outlines optimized process parameters for producing high-quality lines, accompanied by a regression equation for statistically estimating line width [24].

These studies show the advantages of ML, or in better words, data-driven approaches, in determining the quality and dimensions of 3D printed parts based on the process parameters of printing. However, a notable limitation of these methods is that they overlook the underlying physical principles of the printing process. Incorporating these physical principles could lead to significant improvements in predicting the quality and dimensions of the printed parts. Physics Guided Artificial Neural Network (PGANN) is a popular method that bridges the gap between purely data-driven models and traditional physics-based models. This hybrid methodology leverages the predictive power of neural networks while grounding these predictions in the immutable laws of physics, ensuring that the outputs not only fit the observed data but also adhere to known physical behaviors [25]. Amidst this backdrop, we introduce a pipeline that initially identifies whether the selected process parameters—including applied pressure, material viscosity, nozzle diameter, and extruder movement velocity—result in uniform high-quality printing of MXene ink. Subsequently, it predicts the diameter of the MXene filament for the selected set of process parameters using a PGANN that combines the fundamental physics of the printing process with empirical measurements.

Regarding the principles of physics, we derive a physic-based equation from interdisciplinary theories of material properties and fluid dynamics to estimate the diameter of the printed filament given the applied pressure, material viscosity, nozzle diameter, nozzle length, and extruder movement velocity. To determine whether a chosen set of process parameters will lead to high-quality nanomaterial printing, we compared the performance of Random Forest (RF) [26], Extreme Gradient Boosting (XGBoost) [27], and K-Nearest Neighbors (KNN) [28] in classifying the quality of the MXene printings. In the final step, a PGANN based on the approach described in [29] is responsible for predicting the diameter of the MXene filament. This PGANN uses the four process parameters as initial inputs and incorporates the estimation from the introduced physics-based equation as a high-level input. Our comparative study of three types of models — the solely physics-based equation, a solely data-driven Artificial Neural Network (ANN), and the PGANN — indicates that our proposed PGANN model as a holistic approach provides a more physically consistent and

accurate prediction of the printed diameter, compared to methods relying exclusively on either physics-based equation or data-driven approaches. This pipeline blends the physics-based equation with the adaptability of machine learning, equipping researchers and practitioners with an innovative framework that is not only applicable to MXene but also to any advanced nanomaterial ink.

2 Experimental section

2.1 Ink synthesis

The method for preparing the ink draws upon protocols established in our previous work [30]. In brief, we dissolved 1.6 g of lithium fluoride (LiF, 99% purity, supplied by Sigma Aldrich) in 20 mL of 9 M hydrochloric acid (HCl, Sigma Aldrich) through magnetic stirring for 10 min. Following this, we gradually added 1 g of MAX (Ti_3AlC_2, Nanochemazone, Canada) phase powder into the pre-prepared etching solution for 10 min. The etching of the MAX phase was performed at a controlled temperature of 50 °C for an extended period of 30 h. Upon completion of the reaction, the dispersion obtained was subjected to washing with deionized (DI) water, employing repeated centrifugation at 2,700 rpm (1,345 rcf) for 5 min per cycle, until the pH of the supernatant stabilized at approximately 6. The MXene flakes, now self-delaminated, were collected through centrifugation at 1,180 rpm (247 rcf) for 30 min. Subsequently, the dark green supernatant was further centrifuged at 3,500 rpm (2,223 rcf) for 20 min to collect the sediment, which was composed of large MXene flakes and was directly used as ink.

To achieve a final concentration of 4 wt%, 1 mL of the prepared MXene ink was dried, and the remaining solid was weighed. To obtain a broad range of the selected viscosity behavior, the viscosity-tunable ink was achieved by adding and evaporating the water content in the ink mixture, and the weight was measured at each stage to achieve different ink concentrations. In preparation for printing experiments, the ink was homogenized by vortexing for 20 min.

2.2 Ink characterization

The morphological characteristics and thickness distribution of the flakes were analyzed using a scanning electron microscope (SEM, model Quanta FEG 250 from FEI Company). For the analysis, MXene was diluted with deionized water. Following dilution, the MXene ink was uniformly applied to a silica wafer. The coated samples were dried in a hot-air oven, at 60 °C overnight. The determination of flake thickness distribution was based on an assessment of 200 flakes, which were selected from four distinct SEM images. In addition, all Raman spectroscopic data were acquired employing a 532 nm laser as the excitation source (Renishaw, UK).

2.3 Characterization of the rheology behavior

The rheology characterization was conducted on a DHR-2 Rheometer (TA instruments, UK) with the parallel plate geometry for 4, 4.5, and 5 wt% MXene ink to obtain the flow index *n* and consistency index *k* under different ink concentrations. The shear rate was applied from 10^{-2} to 10^{2} (1/s) to simulate the actual change in the shear rate for the 3D-nanomaterial printing system during material extrusion upon 20 points with a uniform increment step.

2.4 Pneumatic extrusion 3D-nanomaterial printing experiment

In this study, we utilized Incredible + 3D bioprinter (Cellink Co, USA), and considering the characteristics of the printer, we selected the feature space of applied pressure (ΔP, 50 – 300 kPa, resolution = 1 kPa), printing velocity (v, 2 – 14 mm/s, resolution = 1 mm/s), and ink concentration (C, 3.8 – 5 wt%). The high-precision dispensing needles (IntelliSpense) were chosen as the nozzle for Pneumatic extrusion 3D-nanomaterial printing. For our micro-resolution printing study, high-precision needles with the smallest inner diameters (*D*) were selected, specifically gauges #27, #30, and #32, with inner diameters of 210, 159, and 108 µm, respectively.

The MXene ink was transferred into new, high-precision cartridges to ensure even flow and prevent solvent evaporation during printing. The cartridges containing the MXene ink were centrifuged at 1000 RPM for 4 min to remove any air bubbles, and then the piston was inserted. The printing process was carried out at room temperature (22 °C).

To thoroughly investigate the potential outcomes of the printing process, we randomly sampled 700 points from the defined feature space of ΔP, v, C, and D. We then conducted line filament printing experiments to document the corresponding printing diameters and qualities, generating a dataset for subsequent analysis. For this experiment, each data point was printed in a straight-line pattern with a length of 2 cm and repeated 3 times.

3 Results and discussion

3.1 Investigation of the physics for pneumatic extrusion 3D-nanomaterial printing process

The cost-effectiveness, rapid prototyping capabilities, and versatility of pneumatic extrusion 3D-nanomaterial printing provide an alternative to the complex steps typically involved in microfabricating devices such as biosensors, flexible circuits, nanoelectronic probes, and nanoneedles [31–34]. Thus, a thorough investigation of the pneumatic extrusion is essential to optimize its performance and ensure precise control over the printed structure. Pneumatic extrusion 3D-nanomaterial printing can be explained in two parts – nanomaterial extrusion and filament deposition [13]. The nanomaterial extrusion describes the ink flow throughout the dispensing nozzle, and the filament deposition depicts the nanomaterial buildup in the printing state. Involving process parameters during printing are applied pressure, nanomaterial viscoelastic property (n for shear thinning index, and k for consistency index), dispensing needle geometry (D for nozzle diameter, and L for nozzle length), and printing velocity (Fig. 1a).

The printing process parameters are directly impacting the material extrusion and filament depositions. For instance, the z-direction flow velocity (V_z), influenced by applied pressure, material viscoelastic properties, and dispensing needle geometry [35], along with the printing head moving speed (v), also known as printing velocity, significantly impacts the quality and diameter of the printed filament. Previous research suggests that v should align with V_z [36] as depicted in Fig. 1b. Based on the principle of flow rate conservation, if v exceeds V_z, the filament diameter will be smaller than the nozzle diameter, leading to filament stretching and non-uniformity. Conversely, if v is less than V_z, the filament diameter will exceed the nozzle diameter, potentially causing material overflow due to excessive accumulation. Therefore, to ensure uniformity, the expected d should align with the nozzle diameter (D), and v should match V_z. According to the development of the modeling for the 3D-nanomaterial printing process, there is no given golden standard to associate all the main printing process parameters to the dimension of the final printed filament. Thus, to optimize the printing parameters, the development of a physics-based model would help understand the influences of different process parameters on the printed filament diameter.

The materials used in pneumatic printing are mainly viscoelastic and may exhibit thixotropy [37]. This complex flow behavior enables the gel ink to behave as a fluid and to present the characteristics of a soft solid material, depending not only on the time scale that they are subjected to perturbations but also on their amplitude. With such property, it enables the smooth nanomaterial extrusion inside the dispensing nozzle to avoid potential clogging and maintains the shape of the printed geometry after extrusion. Such shear thinning behavior can be characterized by two indexes, the shear thinning index (n) and the consistency index (k) from the Ostwald and de Waele power law [38] as the following equation:

$$\eta = k\gamma^{n-1} \tag{1}$$

where η is the apparent viscosity, and γ is the shear rate.

In this study, we utilize MXene ink, a nanomaterial comprising a carbon backbone, transition metals as substituents, and terminal groups serving as anchorage sites (e.g., =O, -F, -OH) [39]. Previous research with MXene inks has highlighted their exceptional conductivity, hydrophilic surfaces, and ease of processing [15, 40]. Both Raman spectroscopy and scanning electron microscopy (SEM) were employed to characterize the MXene nanomaterial.

Raman spectroscopy revealed distinctive features for both MAX and MXene materials. In MAX, prominent peaks at 148.1, 268.5, and 361.2 cm^{-1}, attributed to the vibrations of Al and Ti atoms, were observed (as indicated by the black curve in Fig. 1c) [41]. These peaks correspond to shear and longitudinal modes of vibration [42]. Conversely, following the extraction of Al from the Ti_3AlC_2 powder, the resulting MXene material exhibited weaker Raman signals within the 200 – 700 cm^{-1} range (illustrated by the red curve in Fig. 1c), indicating a reduction in structural integrity and crystallinity. Notably, MXene displayed three distinct Raman bands at 262.6, 397.2, and 608.9 cm^{-1}, with a notable peak at 149.3 cm^{-1} indicative of Ti_3C_2 formation [42, 43]. Also, SEM was employed to examine the surface morphology of MXene. In Fig. 1d, SEM images of MXene revealed clear spaces between layers, confirming the successful removal of Al and indicating the

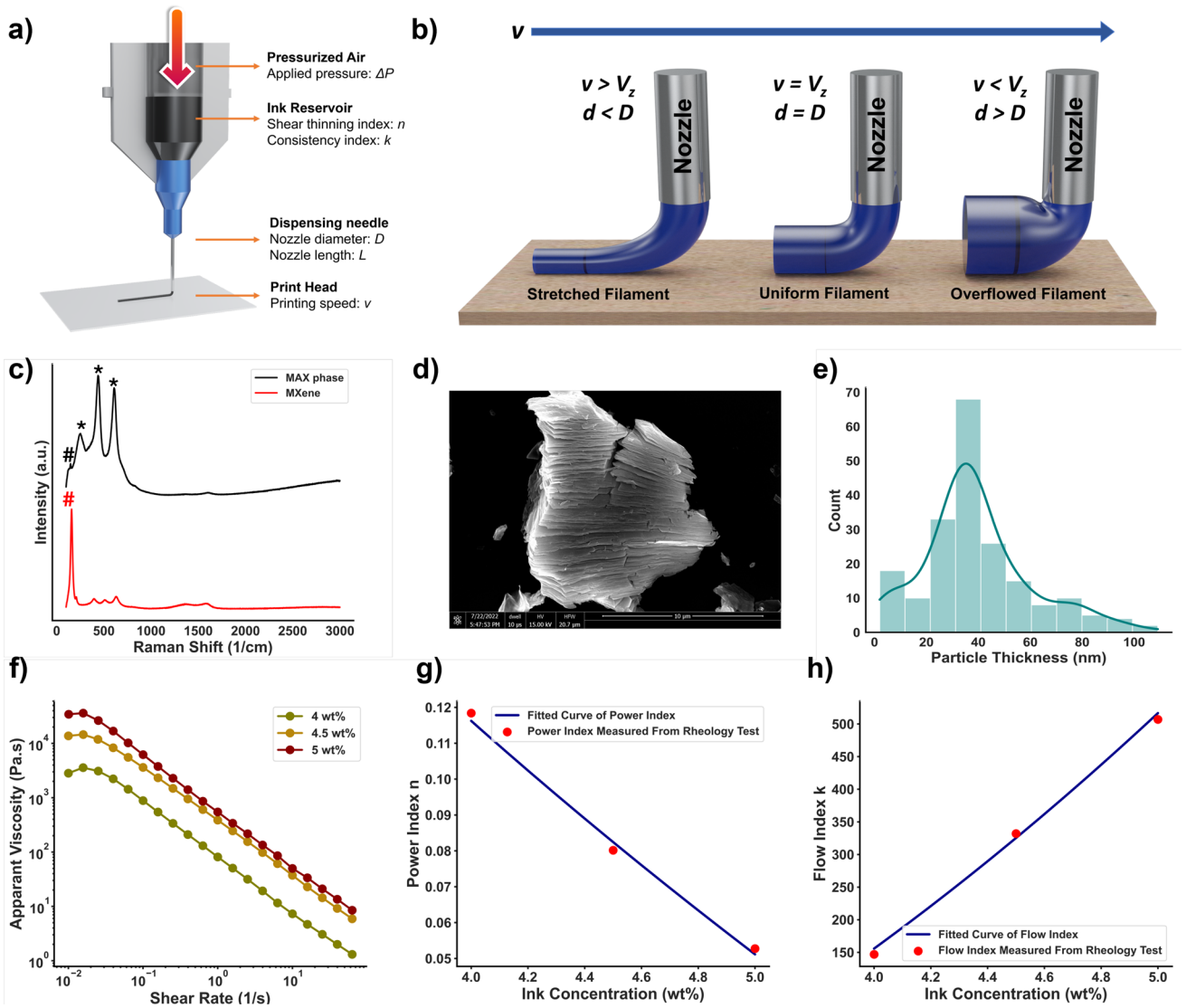

Fig. 1 Printing parameters and MXene ink characterization. **a** Schematic of the pneumatic extrusion 3D-nanomaterial printing process and the critical parameters for printing optimization. *ΔP*: Applied Pressure, *n*: shear thinning index, *k*: consistency index, *D*: nozzle diameter, *L*: nozzle length, *v*: printing speed. **b** The schematic illustration of the filament formation for the competing mechanism between the extrusion speed (*Vz*) and printing head speed (*v*). Stretched Filament: The head speed is larger than the extrusion speed, and the printed diameter is smaller than the nozzle diameter. Uniform Filament: The print head speed is similar to the extrusion speed, and the printed diameter is similar to the nozzle diameter. Overflowed Filament: The moving speed is smaller than the extrusion speed, and the printed diameter is larger than the nozzle diameter. **c** Raman spectroscopy for MAX and MXene materials; MAX with relevant peaks at 148.1, 268.5, and 361.2 cm^{-1} attributed to the vibrations of Al and Ti atoms and MXene with a peak at 149.3 cm^{-1} related to the Ti_3C_2 formation. **d** SEM micrographs of the MXene flakes. **e** Thickness distribution of 200 MXene flakes. **f** Rheology behavior of MXene inks, viscosity plotted as a function of shear rate for different concentrations (4, 4.5, and 5 wt%). **g** The linear fitting curve of the shear thinning index versus ink concentration. **h** The fitting function of the consistency index versus ink concentration

efficient formation of MXene [44]. Furthermore, SEM images were processed to measure the thickness of MXene sheets, yielding an average diameter of 39.24 ± 20.72 nm, thus confirming the nanoscale features of the MXene sheets (Fig. 1e).

Similar to our previous work [30], the MXene inks with different concentrations (4, 4.5, and 5 wt%) were prepared and the viscosity indexes were calculated. As shown in Fig. 1f and Fig. S1, the prepared 3D printable MXene inks showed a typical shear thinning behavior, where the viscosity is high in the low shear rate region and gradually decreases as the shear rate increases. The two main parameters (i.e., *n* and *k*) can be obtained by fitting the data from the rheology test into the power law equation (Eq. 1) for each concentration (Fig. 1g and h). After fitting the obtained data points for different concentrations (C: 4, 4.5, and 5 wt%), the viscosity parameters (i.e., *n* and *k*) followed the equations:

$$n = 1 - 0.56835C^{0.31844} \tag{2}$$

$$k = 43.51203C^2 - 30.76384C - 417.3208 \tag{3}$$

The derived equations for n and k are then applied to determine these parameters for different MXene ink concentrations used in printing.

The deduction process of the pneumatic extrusion 3D-nanomaterial printing flow model starts from the Power Law Model for non-Newtonian fluids [35]:

$$\tau = k\gamma^n \tag{4}$$

The shear rate experienced by the ink in the axial direction can be expressed as [35]:

$$\gamma = \frac{dV_z}{dr} \tag{5}$$

where The shear rate in the axial direction is determined by the velocity V_z at radius r. The shear rate in the axial direction (γ) (Eq. 5) is substituted in (Eq. 4):

$$\tau_{rz} = k\left(\frac{dV_z}{dr}\right)^n \tag{6}$$

Considering that the flow inside the nozzle is laminar, the linear variation of the shear stress across the nozzle cross-section r can be written as [35]:

$$p\left(\pi r^2\right) - (p + \Delta p)\pi r^2 = \tau_{rz} 2\pi r L \tag{7}$$

After simplifying:

$$\tau_{rz} = -\left(\frac{\Delta p}{L}\right)\frac{r}{2} \tag{8}$$

Combining Eqs. 6 and 8, the z-direction flow velocity (V_z) can be expressed as:

$$dV_z = \left\{\left(\frac{-\Delta p}{L}\right)\frac{1}{2k}\right\}^{1/n} r^{1/n} dr \tag{9}$$

Integrate with respect to r to obtain the expression for the velocity distribution:

$$V_z = \left(\frac{n}{n+1}\right)\left\{\left(\frac{-\Delta p}{L}\right)\frac{1}{2k}\right\}^{1/n} r^{(n+1)/n} + constant \tag{10}$$

At the nozzle walls (i.e. when $r = R$), the velocity V_z must be zero to satisfy the no-slip condition. Substituting the value $V_z = 0$, when $r = R$ in Eq. 10, the velocity distribution can be expressed as:

$$V_z = \left(\frac{n}{n+1}\right)\left(\frac{-\Delta p R}{2kL}\right)^{1/n} R\left\{1 - \left(\frac{r}{R}\right)^{\frac{(n+1)}{n}}\right\} \tag{11}$$

The volume flow rate is used to represent the amount of the ink material extrusion rate (dQ) given by:

$$dQ = 2\pi r V_z dr \tag{12}$$

where the extrusion volumetric flow rate is obtained by integration over the cross-section of the nozzle as:

$$Q_{extrusion} = \int_0^R 2\pi r V_z dr \tag{13}$$

For the material deposition stage, the certain filament extruded from the printing nozzle is laid on the printing bed by the controlled movement at a velocity v. Assuming the extruding filament is continuous through the extrusion and maintains a circular shape after the extrusion. $Q_{printing}$ can be defined as:

$$Q_{printing} = \pi d^2 v/4 \tag{14}$$

where d is the diameter of the printed filament and v is the moving speed. Considering the volume is conservation throughout the entire printing process, $Q_{extrusion} = Q_{printing}$, we can calculate the printed filament diameter as:

$$d = \sqrt{\left(\frac{n}{3n+1}\right)\left(\frac{D^3}{2vk^{1/n}}\right)\left(\frac{D\Delta p}{4L}\right)^{1/n}} \tag{15}$$

Utilizing Eq. 15, the diameter of the printed filament (d) can be determined by the other major printing parameters, Δp, v, viscosity parameters (n, k), and D based on the fundamentals of material properties and fluid dynamics. However, the model was based on ideal assumptions, such as the power law fluid, the laminar flow during extrusion, and the incompressible behavior of the ink. In addition, it lacks the interpretation of the circumstances of different printing failures, which frequently occurred in the actual printing experiments. Therefore, more studies should be conducted to obtain a practical, applicable model for optimizing the printing parameters.

3.2 Various printing outcomes and primary visualization of the experimental dataset

As mentioned earlier, changing the printing process parameters may cause non-uniform printing or failures during nanomaterial printing. For optimal parameter configuration, it is important to identify all the different classes of printing outcomes and detect the set of process parameters that result in uniform nanomaterial printing. The data points in our experimental dataset are categorized into four distinct classes: non-extrudable, discrete, uniform, and overflowed printing. Non-extrudable printing fails to produce any filament, as demonstrated in Fig. 2a, while discrete printing produces spaced, short segments that, when closely spaced, resemble a wavy line rather than a uniform extrusion (Fig. 2b). Both the non-extrudable and discrete printing classes are unfavorable as they disrupt the continuity necessary for optimal 3D printing of MXene. Conversely, uniform printing successfully generates a continuous filament (Fig. 2c). The overflowed printing results in the excess deposition of the ink material, which is not controllable (Fig. 2d).

Our visualization of the experimental dataset, supported by 3D Kernel Density Estimate (KDE) plots representing permutations of pressure, velocity, and ink concentration, suggests a statistical likelihood of a shift from continuous, uniform printing (Fig. 2c I-III) to overflowed printing with an increase in applied pressure or a decrease in ink concentration (Fig. 2d I-III). Moreover, Fig. 2a I-III indicates a higher probability of non-extrudable printing outcomes when the pressure is reduced, and ink concentration is increased. The KDE plots for uniform and discrete printing reveal almost similar distributions for these two printing classes, making it challenging to differentiate between them based on their process parameters (Fig. 2b I-III).

Continuing with the visualization of our experimentally collected dataset, Fig. 3a presents a pie chart that illustrates the percentage distribution of each class within the dataset. This chart shows that uniform printing is the most common outcome within the selected process parameters space, representing 48.7% of the dataset. On the other hand, non-extrudable printing is the least common, comprising just 10.9% of the dataset. Additionally, to evaluate potential linear relationships between input features, we computed the Pearson correlation coefficients (PCC) between process parameters. The correlation matrix, presented in Fig. 3b, suggests a negligible linear correlation between each pair of process parameters, with all coefficients being lower than 0.5. This lack of strong correlation suggests that multicollinearity is not a significant concern. Furthermore, within the uniform printing category, Fig. 3c and d showcase the KDEs and box plots for the diameter of uniformly printed filaments, categorized according to their corresponding nozzle diameter. The results indicate a clear trend: an increase in nozzle diameter correlates with an increase in the average width of the printed filament and the diameters of the printed filaments tend to closely mirror their respective nozzle diameter.

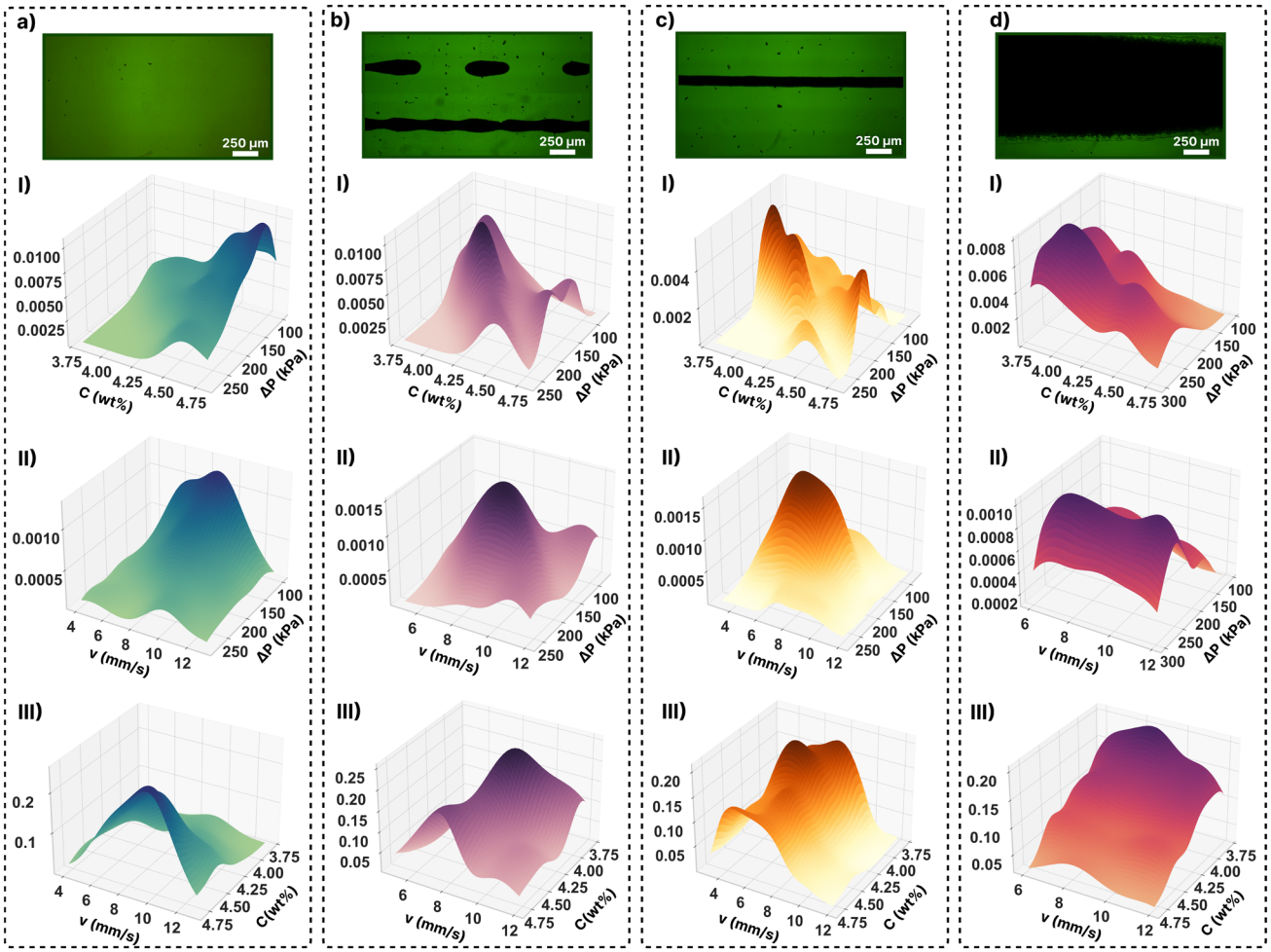

Fig. 2 Optical microscopy images and 3D KDE plots of the various printing quality classes. The optical images demonstrate **a** non-extrudable, **b** discrete, **c** uniform, and **d** overflowed printing results. The corresponding 3D KDE plots **a** I-III, **b** I-III, **c** I-III, and **d** I-III, respectively illustrate the density distribution of printing process parameters — pressure, velocity, and ink concentration — for each printing quality class, offering insights into the parameter space that defines each printing quality class

3.3 Printing quality classification

The visualizations from our experimental dataset give us a sense of the trends that process parameters follow to achieve uniform printing of MXene ink. However, determining the quality of the printed filament from the printing process parameters is a multidimensional problem involving variations and complex interrelationships among applied pressure, ink concentration, nozzle diameter, and printing velocity. To capture the interrelationships between these parameters and accurately detect the quality of the printing filament, we turn to machine learning (ML) as a powerful tool used by researchers in various fields [45, 46].

Three ML models, including Random Forest (RF), Extreme Gradient Boosting (XGBoost), and K-Nearest Neighbors (KNN) are compared in classifying the 4 categories of printing results. Each of these models offers unique structures that enable them to manage interactions between process parameters and perform classification. To comprehensively compare a range of model structures, we selected these three to identify the one that best captures patterns in the training dataset and delivers the highest accuracy. RF was chosen for its capacity to manage complex interactions and resist overfitting, XGBoost for its ability to handle non-linear interactions and patterns, and KNN for its effectiveness in detecting local patterns. In the first step, the dataset was divided into training and testing sets following an 8:2 ratio. The models were then trained on the training set and evaluated on the testing set, which was not exposed to the model beforehand, to determine their capability to generalize to new data [47].

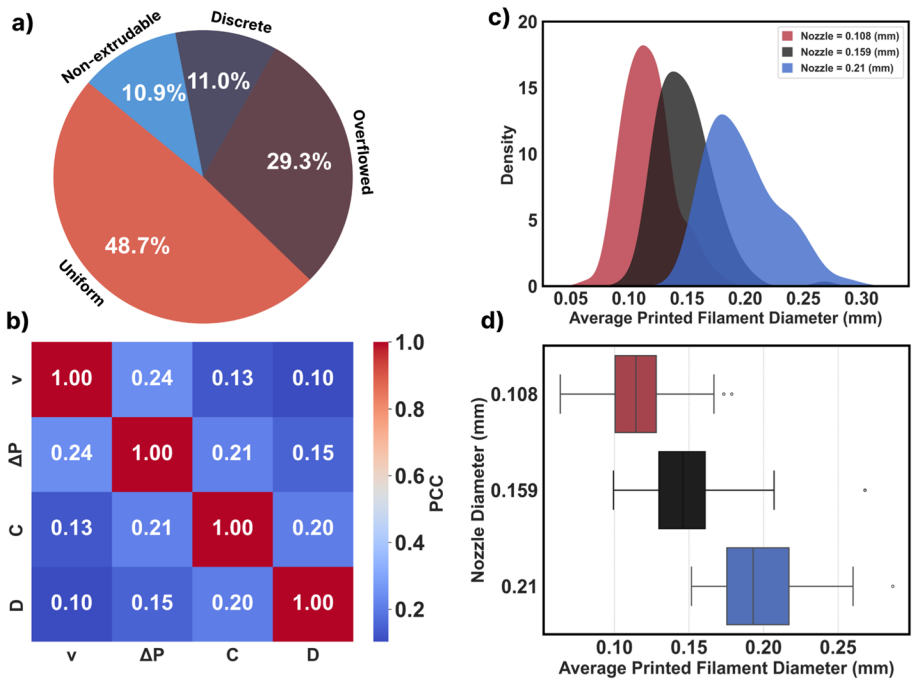

Fig. 3 Comprehensive visualization of experimental dataset. **a** The distribution of printing classes is displayed in a pie chart, indicating that 48.7% of the dataset falls within the 'Uniform' class. **b** The correlation matrix between process parameters — printing velocity (*v*), applied pressure (*ΔP*), ink concentration (*C*), and nozzle diameter (*D*) — shows PCC < 0.5, suggesting minimal multicollinearity concerns. **c** KDE plots for the diameter of uniformly printed filaments, categorized by nozzle diameters of 108, 159, and 210 µm. **d** Box plots of the printed filament diameter, grouped by nozzle diameter, illustrate that the diameters of the uniformly printed filaments generally center around their respective nozzle diameter

For optimal performance from all the ML models, we conduct hyperparameter optimization using the grid search method [48] for the key parameters of each model. Grid search is a thorough method of hyperparameter optimization that iteratively explores the specified range of values for each hyperparameter, constructing and evaluating a model for each possible combination. In addition, we utilize fivefold cross-validation to prevent the optimized hyperparameters from being skewed toward a particular data segment. This robust validation method divides the dataset into five equal parts. The model is trained on four parts and validated on the remaining part, with this process rotating through each part in succession. This ensures the selection of hyperparameters that bolster the overall robustness and performance of the models.

The RF algorithm utilizes an ensemble of decision trees in parallel to improve prediction accuracy and control overfitting. Key hyperparameters include number of estimators, controlling the number of trees and thus model complexity; maximum depth (max_depth), limiting tree depth to prevent overfitting; and minimum samples split (min_samples_split), determining the minimum samples for node splitting [49]. The grid search results for RF (Fig. 4a-d) indicate that prediction accuracy marginally increases with an increase in the number of trees from 5 to 350. However, accuracy stabilizes upon further increasing the number of estimators beyond 350, suggesting that the RF model has reached its developmental limit and does not expand further. Additionally, the results demonstrate that increasing tree depth from 1 to 20 enhances accuracy, but further depth increases do not improve model performance. Conversely, reducing the 'min_samples_split' from 15 to 2 significantly increases accuracy. In conclusion, the highest average accuracy of 83.61% is achieved by an RF model with 'n_estimators' set to 350, 'max_depth' of 20, and 'min_samples_split' of 2.

The KNN algorithm predicts an output by identifying the closest data points in the feature space, utilizing key hyperparameters such as 'n_neighbors', 'weights', and 'algorithm' to significantly influence its performance. The 'n_neighbors' hyperparameter specifies the number of nearest neighbors to be considered. Where a larger number of neighbors can lead to smoother decision boundaries but may result in underfitting. The 'weights' parameter defines the influence of neighbors on the prediction, with 'uniform' treating all neighbors equally, regardless of distance, and 'distance' giving more weight to closer neighbors, enhancing accuracy in densely populated regions. The 'algorithm' hyperparameter selects the computation method for nearest neighbors, including 'ball_tree', and 'kd_tree', which are designed for data with complex structures. The 'ball_tree' constructs a hierarchical structure of nested hyper-spheres to partition the data efficiently, whereas the 'kd_tree', or k-dimensional tree, organizes points in k-dimensional space using binary trees. Lastly, 'brute' performs a comprehensive search through all possible pairs, which is straightforward but computationally demanding [50]. The brute algorithm along with distance-related weights and number of neighbors equal to 18 gives the best accuracy of 64.13% (Fig. 4e and f).

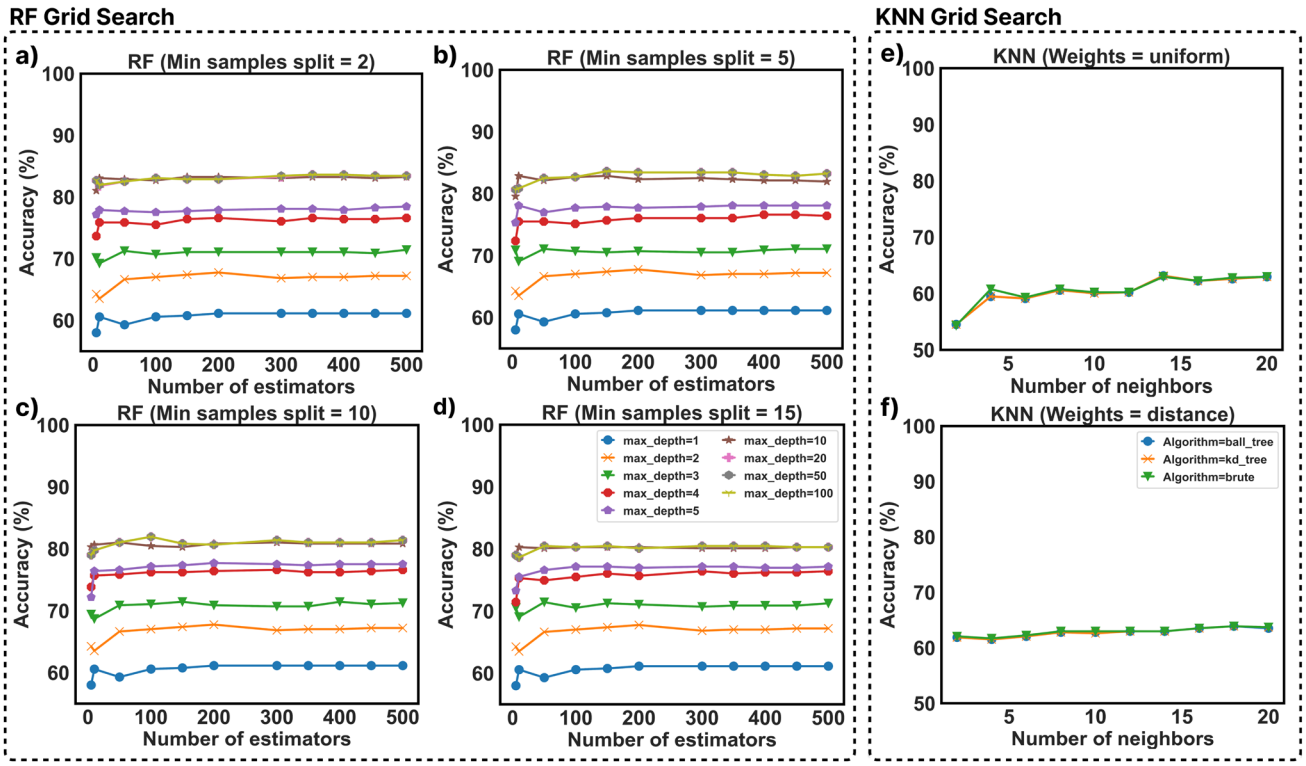

Fig. 4 Optimization of RF and KNN hyperparameters. **a**–**d** RF grid search results displaying the influence of n_estimators, max_depth, and min_samples_split on accuracy, with optimal settings of 350 trees, depth of 20, and a minimum of 2 samples for splitting nodes, achieving 83.61% accuracy. **e**, **f** KNN grid search results indicate that a 'brute' algorithm approach, distance-based weights, and 18 neighbors provide the best performance with 64.13% accuracy

The XGBoost algorithm operates by sequentially building an ensemble of decision trees to correct errors made by previous trees. The number of estimators parameter controls the number of trees in the model, directly impacting its complexity. The learning rate adjusts the influence of each tree on the final outcome, while max_depth determines the maximum depth of the trees [27]. These parameters are crucial for tuning the XGBoost model to achieve a balance between fitting the training data and generalizing well to unseen data. The grid search results for XGBoost (Fig. 5a-d) suggest that an increase in the number of estimators and maximum depth can significantly enhance prediction accuracy. A learning rate of 1 also improved prediction accuracy, as demonstrated in Fig. 5d. Optimal accuracy was achieved with 400 estimators, a maximum tree depth of 1, and a learning rate of 1.

The performance evaluation demonstrates that XGBoost outperforms both RF and KNN in classifying printing conditions on the test dataset as well. This superiority is quantified using four standard evaluation metrics: accuracy, precision, recall, and F1-score, as depicted in Fig. 5e. The confusion matrix in Fig. 5f that comes from the prediction of the optimized XGBoost classifier on the test dataset also shows that the model is 97.62%, 91.43%, 75%, and 75% successful in predicting the Overflowed, Uniform, Discrete, and Non-extrudable samples, respectively.

3.4 Comparative analysis of filament diameter: physics-based equation versus experimental measurements

The physics-based equation presented for estimating uniform filament diameter yields a foundational understanding of the relationship between filament diameter and the process parameters of applied pressure, printing velocity, ink concentration, and nozzle diameter. It is, however, based upon ideal assumptions. This model does not account for non-ideal factors encountered during actual printing, such as the friction between the material and the inner surface of the nozzle. Such friction is negligible only for materials with minimal viscosity, similar to water [51]. Furthermore, additional variables can affect the filament width, including the distance between the dispensing nozzle and the printing stage, and any partial obstruction within the nozzle that could lead to clogging. These non-ideal factors may lead to discrepancies between experimental measurements of filament diameter and the estimates provided by the equation. Here, we assessed the extent of these differences for uniformly printed data points within our experimental dataset.

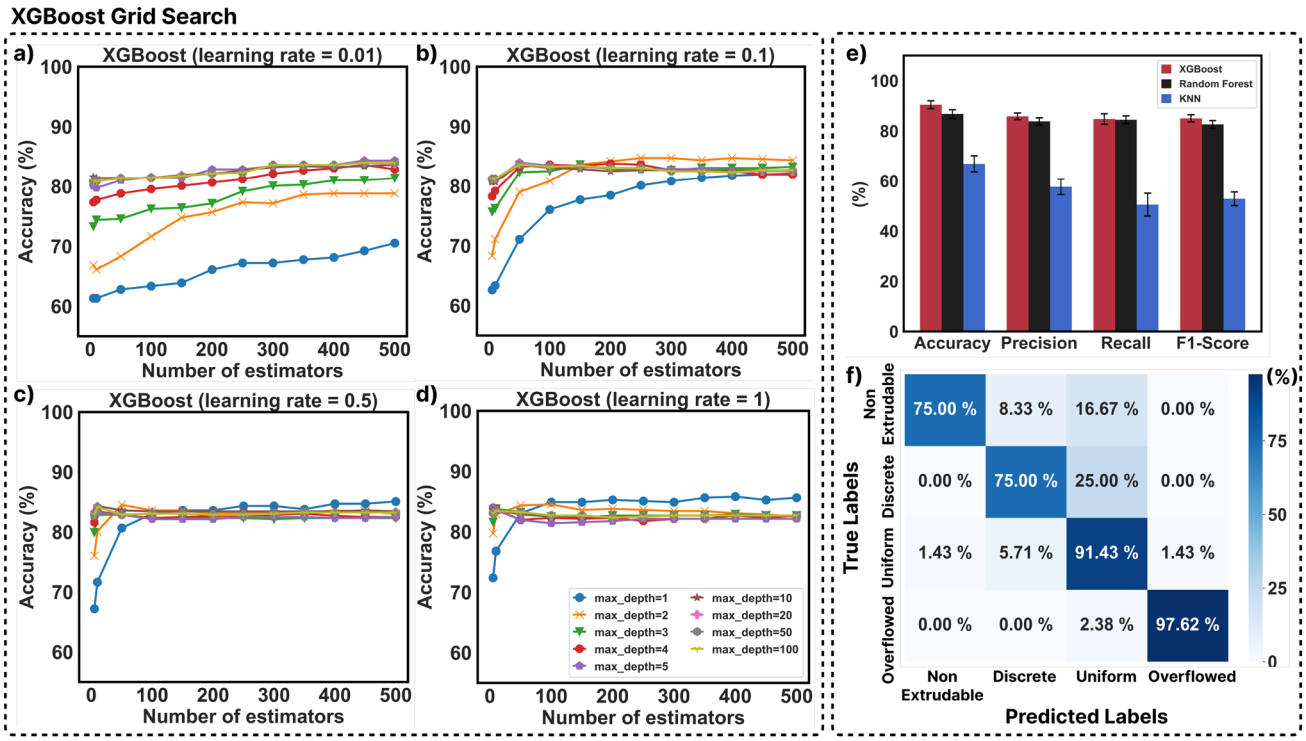

Fig. 5 XGBoost hyperparameters optimization and performance comparison. **a**–**d** Grid search results demonstrating the effect of the number of estimators, learning rate, and max depth on model accuracy, highlighting optimal performance at 400 trees, depth of 1, and learning rate of 1. **e** Comparative analysis of XGBoost, RF, and KNN using accuracy, precision, recall, and F1-score, illustrating XGBoost's superior classification ability with accuracy of 90.44%. **f** Confusion matrix for XGBoost predictions on the test dataset, with high accuracy in identifying different print conditions

Our visualizations confirm a robust positive correlation, with a PCC of 0.83, between the filament widths predicted by the equation and those obtained from experimental measurements (Fig. 6a). This correlation exemplifies the equation's effectiveness in capturing the variability in filament diameter as influenced by the four process parameters: applied pressure, printing velocity, ink concentration, and nozzle diameter. The equation estimations match well with the trends seen in experimental results, showing its ability to account for the complex interactions of the process parameters in determining filament diameter. However, the influence of the non-ideal factors results in the actual measurements of printed diameter being, on average, 0.0494 mm greater than the diameters estimated by the equation for the same set of process parameters (Fig. 6b). The Bland–Altman plot depicted in Fig. 6b further illustrates the limits of agreement, situated at 1.96 times the standard deviation from the mean difference. These limits are defined at -0.0022 mm and -0.0966 mm, respectively, indicating the range within which most differences between the measured and calculated widths are expected to lie. Moreover, the mean absolute error (MAE) and mean squared error (MSE) are determined to be 0.04996 mm and 0.003205 mm^2, respectively.

Although the equation accurately captures the trend of the experimental data, further refinement is needed to decrease the error between the estimated and actual diameter of the printed filament. The experimental observations offer valuable insights into the non-ideal factors not accounted for in the physics-based equation. Therefore, using real-world data could significantly enhance our comprehension of how pressure, velocity, ink concentration, and nozzle diameter interact and influence the outcome.

3.5 Data-driven prediction of filament width

Data-driven approaches stand in contrast to traditional methods by utilizing extensive datasets to reveal underlying patterns and trends [52, 53]. Unlike theoretical approaches, which predominantly rely on idealized assumptions within the problem domain, data-driven strategies aim to unearth hidden patterns in experimental data. This allows for the practical use of experimental outcomes, offering a deeper understanding of real-world phenomena that theoretical models might miss.

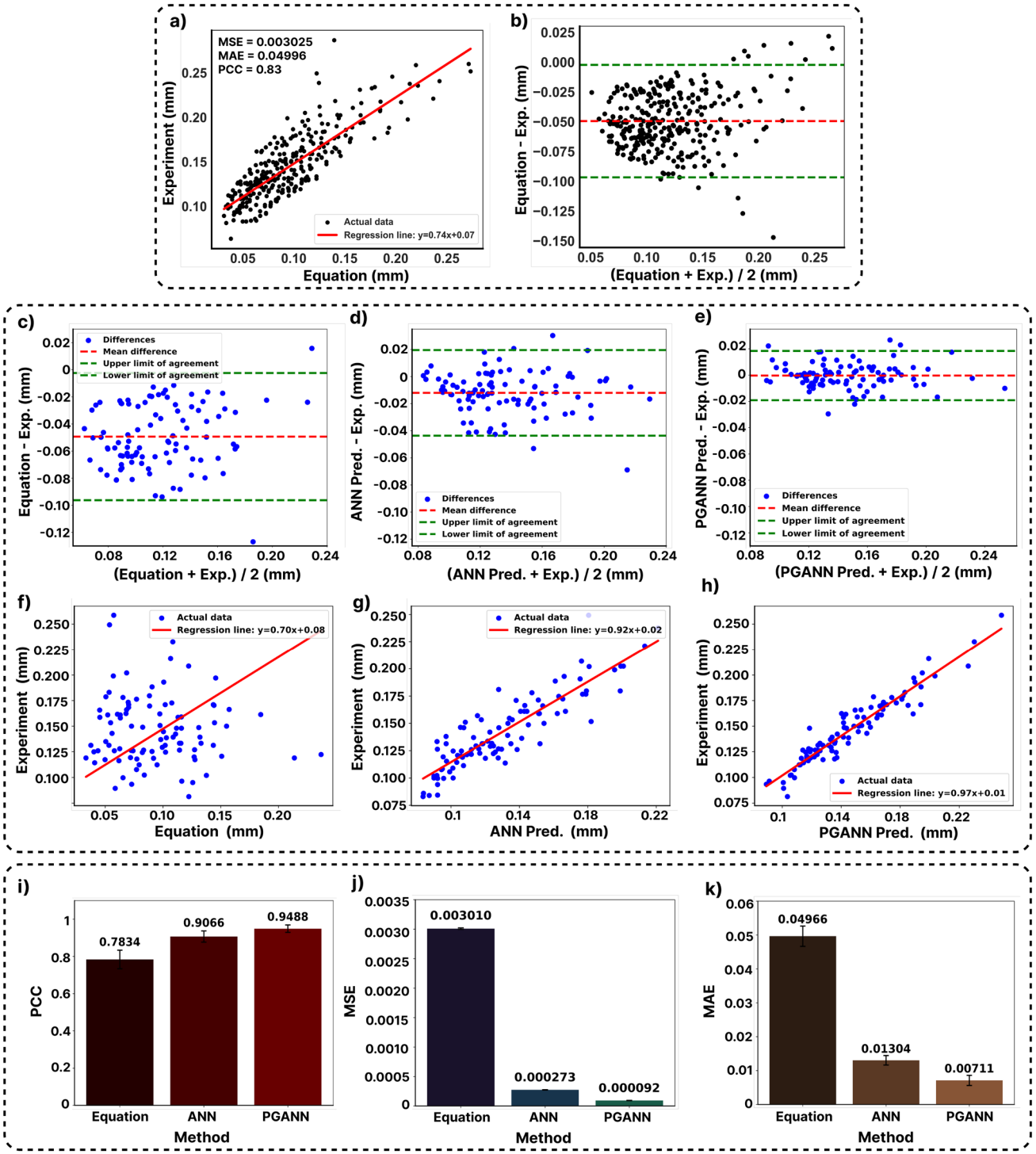

Fig. 6 Comparative analysis of filament diameter predictions versus actual experimental measurements. **a** Regression analysis of filament diameter, comparing experimental measurements with physics-based equation estimations across the full dataset. Indicators include an MSE of 0.003025 mm^2, MAE of 0.04996 mm, and PCC of 0.83. **b** Bland–Altman analysis assessing the agreement between experimental measurements and physics-based equation estimations for filament diameter across the full dataset. **c**–**e** Bland–Altman analysis to compare the differences in filament diameter experimental measurements against predictions from physics-based equation estimations, ANN, and PGANN models within the test dataset. **f**–**h** Regression analysis evaluating the correlation between experimental measurements of filament diameter and predictions from equation estimation, ANN, and PGANN within the test dataset. **i**–**k** Comparative evaluation of PCC, MSE, and MAE values for filament diameter predictions using physics-based equations, ANN, and PGANN methods

In this study, we employed an Artificial Neural Network (ANN) trained on experimental data to predict the diameter of the printed filament using process parameters as the inputs to the ANN. To prepare the ANN, the dataset containing uniform data points was split into training and testing sets in a 70:30 ratio. We constructed a fully connected artificial neural network architecture featuring two hidden layers. A comprehensive grid search was conducted to fine-tune the hyperparameters: the number of nodes in each layer, the activation function for each layer, and the learning rate during training while utilizing the ADAM optimizer for optimization. The search for the optimal number of nodes explored values of (32, 64, 128, 256) for the first layer and (4, 8, 16, 32) for the second layer. Learning rates considered included (0.1, 0.01, 0.001, 0.0001), alongside activation functions (Tanh, ReLU), and batch sizes (8, 16, 32), to determine the most effective combination for accurate printed filament diameter prediction. The outcomes of this grid search (Supplementary Figs. 2 and 3) demonstrate that the ANN model achieves optimal performance with a configuration of 128 nodes in the first layer and 8 nodes in the second layer, utilizing ReLU as the activation function, a batch size of 16, and a learning rate of 0.01.

The analysis of filament diameter predictions made by the optimized ANN demonstrates a notable improvement in the alignment between the predicted and actual filament widths, as evidenced by the testing dataset. The Bland–Altman plots, as illustrated in Fig. 6c and d, reveal a reduction in the mean difference of predictions to -0.00732 mm when using the ANN approach, in contrast to a mean difference of -0.04933 mm resulting from the equation-based estimations for the same dataset. Furthermore, there is a noticeable contraction in the limits of agreement, defined as 1.96 times the standard deviation from the mean difference. This contraction is evident when compared to the broader limits observed for the differences derived from the physics-based equation estimations. These results not only highlight the superior accuracy of the ANN in predicting filament widths but also reflect its efficacy in closely mirroring actual experimental outcomes.

The regression analysis comparing ANN predictions and equation-based estimations against actual experimental measurements, as presented in Fig. 6f and g, reveals a more pronounced correlation for the ANN model, with a PCC of 0.9066, versus the equation model's PCC of 0.7834 (Fig. 6i). In terms of error metrics on the test dataset, the ANN model registers substantially lower values with an MSE of 0.000092 mm^2 and an MAE of 0.00711 mm—significantly outperforming the physics-based equation by factors of 11 and 4, respectively (Fig. 6j and k).

3.6 Physics-guided artificial neural network (PGANN) for prediction of filament diameter

While the ANN, as a data-driven approach, shows superior performance in predicting filament diameter based on the four process parameters, it lacks the insights that can be provided by a physics-based equation, specifically in constraining its output to a manifold of physically realizable models. Therefore, there is a need for a model that integrates the knowledge from physics with the insights of our data-driven approach to improve predictions and reduce the error between predicted and experimental results.

In the PGANN framework, the ANN is augmented with the output of the ideal physics-based model. PGANN utilizes the optimized ANN described in Sect. 3.5 to learn the latent representation of the four input process parameters. This latent representation is further augmented with the output of the physics-based model for the printed diameter filament at a third layer (intermediate layer), which contains 8 nodes and uses a ReLU activation function. The training of PGANN is performed using the Adam Optimizer with a learning rate of 0.01 and a batch size of 16.

The predictions made by the PGANN on the test dataset significantly enhance the agreement between the predicted and actual filament diameters. The Bland–Altman plot depicted in Fig. 6e highlights a mean difference of 0.0011679 mm between the actual printed filaments and the PGANN predictions, showing a notable improvement over the mean difference of -0.00732 mm achieved with the ANN approach. Furthermore, the distance between the 1.96 limits of agreement has reduced from 0.093864 mm to 0.038007 mm, demonstrating a higher accuracy and reduced variability compared to ANN predictions.

Also, regression analysis of the PGANN predictions against actual experimental measurements, as shown in Fig. 6h, demonstrates a stronger correlation for the PGANN model, with a PCC of 0.9488, compared to the ANN model's PCC of 0.9066 (Fig. 6i). Regarding error metrics on the test dataset, the PGANN model exhibits significantly lower values than those derived solely from physics-based equations or purely data-driven predictions (i.e. ANN), recording an MSE of 0.000273 mm^2 and an MAE of 0.00711 mm. This performance substantially surpasses that of the ANN model, as illustrated in Fig. 6j and k.

3.7 Experimental validation of the prediction of filament width

In order to test the predictive capabilities of our model, we conducted an experiment using four different sets of parameters to predict the printed outcomes using a 0.159 µm nozzle (Fig. 7). After printing, we carried out experiments using the specified parameters and captured the results in photographs (Fig. 7a, b). Our model accurately predicted the printed output for discrete, continuous, and overflowed lines. We also used smaller and larger nozzles with diameters of 0.108 µm and 0.210 µm, respectively, to validate the prediction system (Figs. S3 and S4). The results of these tests can be found in

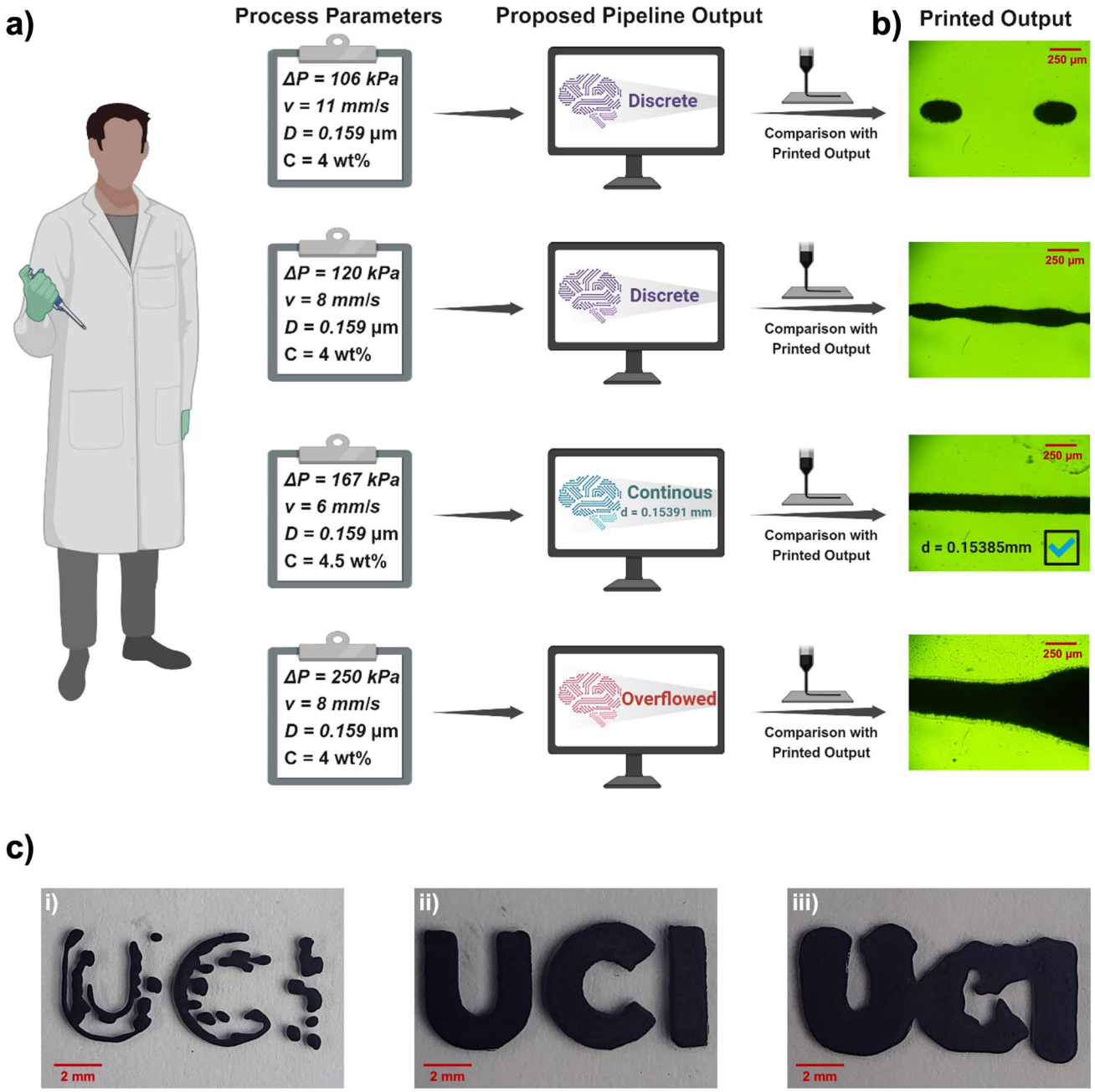

Fig. 7 Overview of the 3D printing using a 0.159 µm nozzle under varying process parameters. **a** Four different sets of process parameters (pressure, velocity, diameter, and concentration) were tested, with the predicted outcomes classified as discrete, continuous, or overflowed. **b** Experimental results showing the printed line thickness corresponding to each set of parameters, with the measured thickness indicated for the continuous printing case (Scale Bar = 250 µm). **c** Printing the UCI logo using the same process parameters resulted in three distinct outcomes: **i** discrete printing, **ii** continuous printing, and **iii** overflowed printing (Scale Bar = 2 mm)

the supplementary file. Additionally, we created an STL model of the UCI logo and used the same parameters for printing (Fig. 7c), which resulted in three distinct printing outcomes.

4 Conclusion

In this study, we developed a comprehensive pipeline designed to assist researchers in optimizing process parameters for Pneumatic Extrusion 3D nanomaterial extrusion printing. This pipeline is specifically tailored to meet the demands for uniform, high-quality printing with desired resolutions. We focused on the application of this pipeline to the printing of MXene ink, a 2D transition nanomaterial known for its potential in nano-energy production, flexible electronics, and wearable sensors. Given MXene's requirements for precise filament diameter control, our pipeline is crucial for producing uniform, conductive, and microscale components.

This pipeline includes an XGBoost classifier that can determine the quality of MXene ink prints based on pre-selected process parameters with an accuracy of 90.44%. Additionally, we derived a physics-based model from material properties and fluid dynamics theories to estimate filament diameter, providing a clear understanding of how filament diameter is influenced by process parameters. This physics-based equation is integrated into a PGANN to enhance prediction accuracy and minimize discrepancies between predicted and experimental results. The PGANN model demonstrates superior predictive capability, achieving a PCC of 0.9488, an MSE of 0.000273 mm^2, and an MAE of 0.00711 mm. This pipeline enables researchers to select optimal printing parameters more efficiently, ensuring consistently high-quality prints and precise filament diameters.

Acknowledgements This work was supported by the start-up funds provided to R.E. by the Henry Samueli School of Engineering and the Department of Electrical Engineering at the University of California, Irvine.

Author contributions R.E—conceived the idea, and designed research and experiments and supervised the study; A.G, J.A.T, and Q.Y—performed experiments with assistance from J.R; A.G—performed the formal analysis, investigations, and visualizations; A.G, and J.A.T—drafted the paper; R.E, A.G, J.A.T, J.R, Q.Y—reviewed the paper and provided feedback.

Data availability Data sets generated during the current study are available from the corresponding author upon reasonable request.

Code availability The source code is available from the corresponding author upon reasonable request.

Declarations

Competing interests The authors declare no competing interests.

Ethical approval On behalf of all authors, the corresponding author affirms that this research article did not involve any human or animal studies.

References

1. NajafiKhoshnoo S, Kim T, Tavares-Negrete JA, Pei X, Das P, Lee SW, Rajendran J, Esfandyarpour R. A 3D nanomaterials-printed wearable, battery-free, biocompatible, flexible, and wireless ph sensor system for real-time health monitoring. Adv Mater Technol. 2023;8:2201655.
2. Tavares-Negrete JA, Babayigit C, Najafikoshnoo S, Lee SW, Boyraz O, Esfandyarpour R. A novel 3D-bioprinting technology of orderly extruded multi-materials via photopolymerization. Advanced Materials Technologies. 2023;8:2201926.
3. Kim T, Yi Q, Hoang E, Esfandyarpour R. A 3D printed wearable bioelectronic patch for multi-sensing and in situ sweat electrolyte monitoring. Advanced Materials Technologies. 2021;6:2001021.
4. Esfandyarpour R, Esfandyarpour H, Harris JS, Davis RW. Simulation and fabrication of a new novel 3D injectable biosensor for high throughput genomics and proteomics in a lab-on-a-chip device. Nanotechnology. 2013;24: 465301.

5. Matias ML, Pereira C, Almeida HV, Jana S, Panigrahi S, Menda UD, Nunes D, Fortunato E, Martins R, Nandy S. 3D printed MXene architectures for a plethora of smart applications. Materials Today Advances. 2024;23: 100512.
6. Zhu G, Zhang H, Lu J, Hou Y, Liu P, Dong S, Pang H, Zhang Y. 3D printing of mxene-enhanced ferroelectric polymer for ultrastable zinc anodes. Adv Func Mater. 2024;34:2305550.
7. Chakoma S, Pei X, Qin H, Ghandehari A, Najafikhoshnoo S, Rajendran J, Esfandyarpour R. A passive, reusable, and resonating wearable sensing system for on-demand, non-invasive, and wireless molecular stress biomarker detection. Nano Res. 2024;17(8):7542–56. https://doi.org/10.1007/s12274-024-6738-7.
8. Das P, Najafikhoshnoo S, Tavares-Negrete JA, Yi Q, Esfandyarpour R. An in-vivo-mimicking 3D lung cancer-on-a-chip model to study the effect of external stimulus on the progress and inhibition of cancer metastasis. Bioprinting. 2022;28: e00243.
9. Joshi K, Velasco V, Esfandyarpour R. A low-cost, disposable and portable inkjet-printed biochip for the developing world. Sensors. 2020;20:3593.
10. Mazrouei R, Velasco V, Esfandyarpour R. 3D-bioprinted all-inclusive bioanalytical platforms for cell studies. Sci Rep. 2020;10:14669.
11. Tetik H, Orangi J, Yang G, Zhao K, Mujib SB, Singh G, Beidaghi M, Lin D. 3D printed MXene aerogels with truly 3D macrostructure and highly engineered microstructure for enhanced electrical and electrochemical performance. Adv Mater. 2022;34:2104980.
12. Zhou W, Zhou Z, Guo S, Fan Y, Nomura N. Structural evolution mechanism during 3D printing of MXene-reinforced metal matrix composites. Composites Communications. 2022;29: 101034.
13. Suntornnond R, Tan EY, An J, Chua CK. A mathematical model on the resolution of extrusion bioprinting for the development of new bioinks. Materials. 2016;9(9):756.
14. Esfandyarpour R, Yang L, Koochak Z, Harris JS, Davis RW. Nanoelectronic three-dimensional (3D) nanotip sensing array for real-time, sensitive, label-free sequence specific detection of nucleic acids. Biomed Microdevice. 2016;18:1–10.
15. Yi Q, Najafikhoshnoo S, Das P, Noh S, Hoang E, Kim T, Esfandyarpour RJAMT. All-3D-Printed. Flexible, and Hybrid Wearable Bioelectronic Tactile Sensors Using Biocompatible Nanocomposites for Health Monitoring. 2022;7:2101034.
16. J. Bruneaux, D. Therriault, M.-C.J.J.o.M. Heuzey, Microengineering, Micro-extrusion of organic inks for direct-write assembly, 18 (2008) 115020.
17. Cheng J, Lin F, Liu H, Yan Y, Wang X, Zhang R, Xiong Z. Rheological properties of cell-hydrogel composites extruding through small-diameter tips. J Manuf Sci Eng. 2008. https://doi.org/10.1115/1.2896215.
18. Lee JM, Yeong WYJV, Prototyping P. A preliminary model of time-pressure dispensing system for bioprinting based on printing and material parameters: This paper reports a method to predict and control the width of hydrogel filament for bioprinting applications. 2015;10:3–8.
19. A.K. Miri, I. Mirzaee, S. Hassan, S.M. Oskui, D. Nieto, A. Khademhosseini, Y.S.J.L.o.a.C. Zhang, Effective bioprinting resolution in tissue model fabrication, 19 (2019).
20. T.T. Nikam, D.A. Purane, K.M. Kulkarni, Optimization of 3D Printing Process, IARJSET, (2019).
21. Zhouquan Fu, Angeline V, Sun W. Evaluation of printing parameters on 3D extrusion printing of pluronic hydrogels and machine learning guided parameter recommendation. International Journal of Bioprinting. 2024;7(4):434. https://doi.org/10.18063/ijb.v7i4.434.
22. Tamir TS, Xiong G, Fang Q, Yang Y, Shen Z, Zhou M, Jiang J. Machine-learning-based monitoring and optimization of processing parameters in 3D printing. Int J Comput Integr Manuf. 2023;36:1362–78.
23. Deswal S, Narang R, Chhabra D. Modeling and parametric optimization of FDM 3D printing process using hybrid techniques for enhancing dimensional preciseness. International Journal on Interactive Design and Manufacturing (IJIDeM). 2019;13:1197–214.
24. Jeong H, Lee JH, Kim S, Han S, Moon H, Song J-Y, Park A-Y. Optimization of process parameters in micro-scale pneumatic aerosol jet printing for high-yield precise electrodes. Sci Rep. 2023;13:21297.
25. Robinson H, Pawar S, Rasheed A, San O. Physics guided neural networks for modelling of non-linear dynamics. Neural Netw. 2022;154:333–45.
26. Breiman L. Random Forests. Mach Learn. 2001;45:5–32.
27. T. Chen, C. Guestrin, Xgboost: A scalable tree boosting system, In: Proceedings of the 22nd acm sigkdd international conference on knowledge discovery and data mining, 2016, pp. 785–794.
28. Guo G, Wang H, Bell D, Bi Y, Greer K, KNN model-based approach in classification, On The Move to Meaningful Internet Systems,. CoopIS, DOA, and ODBASE: OTM Confederated International Conferences, CoopIS, DOA, and ODBASE 2003, Catania, Sicily, Italy, November 3–7, 2003. Proceedings, Springer. 2003;2003:986–96.
29. Pawar S, San O, Aksoylu B, Rasheed A, Kvamsdal T. Physics guided machine learning using simplified theories. Phys Fluids. 2021. https://doi.org/10.1063/5.0038929.
30. Yi Q, Pei X, Das P, Qin H, Lee SW, Esfandyarpour R. A self-powered triboelectric MXene-based 3D-printed wearable physiological biosignal sensing system for on-demand, wireless, and real-time health monitoring. Nano Energy. 2022;1(101):107511.
31. J. Rajendran, R. Esfandyarpour, Revolutionizing Personalized Health: The Frontier of Wearable Biomolecule Sensors Through 3D Printing Innovation, Biomedical Materials & Devices, (2024) 1–17.
32. Velasco V, Joshi K, Chen J, Esfandyarpour R. Personalized drug efficacy monitoring chip. Anal Chem. 2019;91:14927–35.
33. Esfandyarpour R, Javanmard M, Koochak Z, Esfandyarpour H, Harris JS, Davis RW. Label-free electronic probing of nucleic acids and proteins at the nanoscale using the nanoneedle biosensor. Biomicrofluidics. 2013. https://doi.org/10.1063/1.4817771.
34. Esfandyarpour R, Javanmard M, Koochak Z, Esfandyarpour H, Harris JS, Davis RW. Thin film nanoelectronic probe for protein detection. MRS Online Proc Libr. 2013;1572:1–6.
35. R.P. Chhabra, J.F. Richardson, Non-Newtonian flow and applied rheology: engineering applications, Butterworth-Heinemann2011.
36. Khalil S, Sun W. Biopolymer deposition for freeform fabrication of hydrogel tissue constructs. Mater Sci Eng, C. 2007;27(3):469–78.
37. Chen M, Liu B, Li L, Cao L, Huang Y, Wang S, Zhao P, Lu L, Cheng X. Rheological parameters, thixotropy and creep of 3D-printed calcium sulfoaluminate cement composites modified by bentonite. Compos B Eng. 2020;1(186):107821.
38. Zhang C, Hatzell KB, Boota M, Dyatkin B, Beidaghi M, Long D, Qiao W, Kumbur EC, Gogotsi YJC. Highly porous carbon spheres for electrochemical capacitors and capacitive flowable suspension electrodes. 2014;77:155–64.
39. Lim KRG, Shekhirev M, Wyatt BC, Anasori B, Gogotsi Y, Seh ZW. Fundamentals of MXene synthesis. Nature Synthesis. 2022;1:601–14.

40. Lee SW, Pei X, Rajendran J, Esfandyarpour R. A Wireless and Battery-Free Wearable Pressure Sensing System for Human-Machine Interaction and Health Monitoring. IEEE Journal on Flexible Electronics. 2023;2:439–47.
41. Sarycheva A, Gogotsi Y. Raman spectroscopy analysis of the structure and surface chemistry of Ti3C2T x MXene. Chem Mater. 2020;32:3480–8.
42. Soundiraraju B, George BK. Two-dimensional titanium nitride (Ti2N) MXene: synthesis, characterization, and potential application as surface-enhanced Raman scattering substrate. ACS Nano. 2017;11:8892–900.
43. Berger E, Lv Z-P, Komsa H-P. Raman spectra of 2D titanium carbide MXene from machine-learning force field molecular dynamics. Journal of Materials Chemistry C. 2023;11:1311–9.
44. Wang L, Zhang H, Wang B, Shen C, Zhang C, Hu Q, Zhou A, Liu B. Synthesis and electrochemical performance of Ti 3 C 2 T x with hydrothermal process. Electron Mater Lett. 2016;12:702–10.
45. S. Shirvani, Electric vehicles and charging infrastructure security, (2023).
46. A. Ghandehari, S. Shirvani, H. Moradi, Evaluating the Impact of Traveling on COVID-19 Prevalence and Predicting the New Confirmed Cases According to the Travel Rate Using Machine Learning: A Case Study in Iran, 2021 11th International Conference on Computer Engineering and Knowledge (ICCKE), 2021, pp. 290–295.
47. Okazaki Y, Okazaki S, Asamoto S, Yamaji T, Ishige M. Estimator for generalization performance of machine learning model trained by biased data collected from multiple references. Computer-Aided Civil and Infrastructure Engineering. 2023;38:2145–62.
48. Shekar BH, Dagnew G. Grid search-based hyperparameter tuning and classification of microarray cancer data. In: 2019 second international conference on advanced computational and communication paradigms (ICACCP) 2019 Feb 25 (pp. 1-8). IEEE.
49. Probst P, Wright MN, Boulesteix AL. Hyperparameters and tuning strategies for random forest. Wiley Interdisciplinary Reviews: data mining and knowledge discovery. 2019;9: e1301.
50. Yang L, Shami A. On hyperparameter optimization of machine learning algorithms: Theory and practice. Neurocomputing. 2020;415:295–316.
51. A.C. Yunus, Fluid Mechanics: Fundamentals And Applications (Si Units), Tata McGraw Hill Education Private Limited2010.
52. S. Shirvani, A. Ghorbani, A Study of Ev-Evse Ecosystem Integrity: Machine Learning Based Security Monitoring of Charging Sessions, Available at SSRN 4711137.
53. Chen H, Liu Y, Balabani S, Hirayama R, Huang J. Machine learning in predicting printable biomaterial formulations for direct ink writing. Research. 2023;6:0197.